The EMBO Journal (2006) 25, 1611–1622 | © 2006 European Molecular Biology Organization | All Rights Reserved 0261-4189/06
www.embojournal.org

THE EMBO JOURNAL

SH3P7/mAbp1 deficiency leads to tissue and behavioral abnormalities and impaired vesicle transport

Sabine Connert[1,6,7], Simone Wienand[2,6], Cora Thiel[2,6], Maria Krikunova[3,8], Nataliya Glyvuk[3], Yaroslav Tsytsyura[3], Denise Hilfiker-Kleiner[4], Jörg W Bartsch[5,9], Jürgen Klingauf[3] and Jürgen Wienands[2,*]

[1]Department of Biochemistry and Molecular Immunology, University of Bielefeld, Bielefeld, Germany, [2]Cellular and Molecular Immunology, Medical Faculty of Georg-August-University, Göttingen, Germany, [3]Department of Membrane Biophysics, Max Planck Institute for Biophysical Chemistry, Göttingen, Germany, [4]Cardiology and Angiology, Medical School Hannover, Hannover, Germany and [5]Department of Developmental Biology and Molecular Pathology, University of Bielefeld, Bielefeld, Germany

The intracellular adaptor protein SH3P7 is the mammalian ortholog of yeast actin-binding protein 1 and thus alternatively named as mAbp1 (or HIP55). Structural properties, biochemical analysis of its interaction partners and siRNA studies implicated mAbp1 as an accessory protein in clathrin-mediated endocytosis (CME). Here, we describe the generation and characterization of mice deficient for SH3P7/mAbp1 owing to targeted gene disruption in embryonic stem cells. Mutant animals are viable and fertile without obvious deficits during the first weeks of life. Abnormal structure and function of organs including the spleen, heart, and lung is observed at about 3 months of age in both heterozygous and homozygous mouse mutants. A moderate reduction of both receptor-mediated and synaptic endocytosis is observed in embryonic fibroblasts and in synapses of hippocampal neurons, respectively. Recycling of synaptic vesicles in hippocampal boutons is severely impaired and delayed four-fold. The presynaptic defect of SH3P7/mAbp1 mouse mutants is associated with their constricted physical capabilities and disturbed neuromotoric behaviour. Our data reveal a nonredundant role of SH3P7/mAbp1 in CME and places its function downstream of vesicle fission.

The EMBO Journal (2006) **25,** 1611–1622. doi:10.1038/sj.emboj.7601053; Published online 6 April 2006

*Corresponding author. Department of Cellular and Molecular Immunology, Medical Faculty of the Georg-August-University of Göttingen, Humboldtallee 34, 37073 Göttingen, Germany.
Tel.: +49 551 39 5812; Fax: +49 551 39 5843;
E-mail: jwienan@uni-goettingen.de
[6]These authors contributed equally to this work
[7]Present address: Clinical Research Unit for Rheumatology, University Hospital Freiburg, Freiburg, Germany
[8]Present address: Institute of Experimental Physics, University of Hamburg, Hamburg, Germany
[9]Present address: Department of Biochemistry, King's College London, London, UK

Received: 16 August 2005; accepted: 28 February 2006; published online: 6 April 2006

Subject Categories: membrane & transport; neuroscience
Keywords: actin-binding proteins; clathrin-mediated endocytosis; fluorescence microscopy; SH3P7/mAbp1 deficiency; synaptic vesicle recycling

Introduction

Intracellular components of the endocytic machinery control and regulate multimerization of clathrin triscelia for internalization of soluble and membrane-bound molecules or vesicle recycling in synaptic nerve terminals (Hirst and Robinson, 1998). Initiation of clathrin coat formation is regulated by clathrin-binding proteins such as the β2-adaptin component of the multimeric AP2 complex, which provides a direct link to membranes and membrane receptors (Kirchhausen, 1999; Slepnev and De Camilli, 2000). Vesicle fission from the donor membrane requires a member of the dynamin family of large GTPases (Danino and Hinshaw, 2001). A plethora of clathrin accessory proteins has been identified to assist coat formation and coat dynamics in a regulatable manner (Marsh and McMahon, 1999; Slepnev and De Camilli, 2000). Recently, the intracellular adaptor protein Src homology (SH)3P7 (Larbolette *et al*, 1999) (also named HIP55) (Ensenat *et al*, 1999), which was found to represent the mammalian ortholog of yeast actin-binding protein 1 (Abp1) (Kessels *et al*, 2000), has been added to this list.

Mammalian Abp1 (mAbp1) is expressed in many cell types and possesses a relative molecular mass of 55 kDa. It was initially identified as a protein tyrosine kinase substrate colocalizing with the F-actin cytoskeleton in antigen receptor-stimulated lymphocytes (Larbolette *et al*, 1999). Abp1 binds F-actin with a stoichiometry of 1:5 by virtue of its N-terminal ADFH domain (Lappalainen *et al*, 1998) and an adjacently located charged region with a tetrameric repeat of the consensus sequence R/KXEEXR (Larbolette *et al*, 1999; Kessels *et al*, 2000). The two independent actin-binding modules are followed C-terminally by a putative proline-rich recognition motif for SH3 domains and two known tyrosine-phosphorylation motifs, which provide phospho-acceptor sites for activated Src and Syk family kinases (Lock *et al*, 1998; Larbolette *et al*, 1999). The C-terminus of mAbp1 encompasses an SH3 domain, which allowed the initial cloning of the *mabp1* cDNA (Sparks *et al*, 1996). Several ligands for the mAbp1 SH3 domain have been identified; for example, the hematopoietic progenitor kinase 1 (Ensenat *et al*, 1999) and the huntingtin-interacting protein, Hip1R (S Connert, S Wienand and J Wienands, unpublished results). Furthermore, several neuronally expressed proteins interact with the mAbp1 SH3 domain, most notably presynaptic proteins implicated in clathrin-mediated synaptic vesicle endocytosis and recycling, such as synaptojanin1,

©2006 European Molecular Biology Organization

synapsin1, the vesicle fission-driving dynamin1 (Kessels *et al*, 2001), and piccolo, a scaffolding cytoskeletal matrix protein of the active zone (AZ) (Fenster *et al*, 2003). Also, the postsynaptic multidomain adaptor proteins ProSAP1 and ProSAP2 are mAbp1-associated proteins (Qualmann *et al*, 2004).

Overexpression studies in Cos-7 cells (Kessels *et al*, 2001) and siRNA-mediated knockdown experiments (Han *et al*, 2003; Mise-Omata *et al*, 2003; Le Bras *et al*, 2004) revealed a regulatory role for mAbp1 on transferrin receptor uptake and TCR internalization, supporting the idea that mAbp1 is a key regulator in receptor-mediated endocytosis and vesicle trafficking. This is also evident from biochemical and genetic studies on yeast Abp1. For example, the proline-rich region of Abp1 recruits the SH3 domain of Rvs167/amphiphysin (Lila and Drubin, 1997), which belongs to a protein family engaged in early events of endocytosis, for example, membrane curvature (Takei *et al*, 1999; Peter *et al*, 2004). Lack of Abp1 expression in yeast becomes lethal upon additional loss of the Sla2 protein (for: synthetically lethal with *abp1*) (Holtzman *et al*, 1993). Sla2 protein is essential for both endocytosis and actin function (Holtzman *et al*, 1993; Wesp *et al*, 1997; Yang *et al*, 1999). The mammalian ortholog of Sla2 protein is Hip1R (Seki *et al*, 1998), which we identified as a mAbp1-binding protein (see above). So far, however, a detailed functional analysis of mAbp1 in primary mammalian cells is missing.

Here we present the characterization of mouse mutants rendered deficient for the expression of mAbp1 by gene targeting. Although initially normal, mAbp1-negative mice develop several organ abnormalities including splenomegaly, a four-chamber dilation of the heart and lung emphysema. On the molecular level, clathrin-mediated uptake of fluorescent markers in fibroblasts and hippocampal neurons is slightly reduced. A dramatic defect is observed for the reformation of fusion-competent vesicles in synapses, which can explain the severe behavioral deficits in mAbp1-negative mice.

Results

Targeted disruption of mabp1

A targeting vector was generated, which upon homologous recombination in BALB/c embryonic stem (ES) cells deleted exons 2 and 3 of the *mabp1* gene (Figure 1A). Following neomycin selection, ES cells harboring homologous integration were identified by Southern blot analysis using three different probes A–C (Figure 1A) and subsequently injected

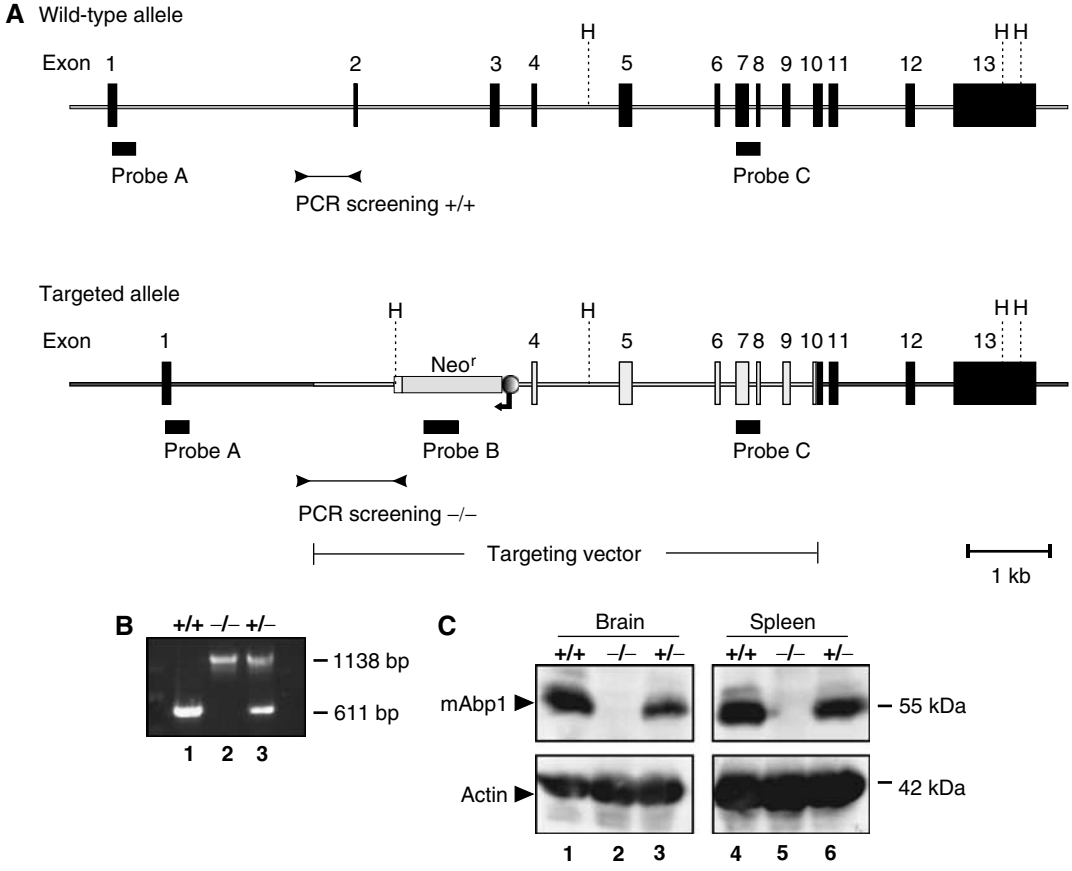

Figure 1 Targeted disruption of murine *mabp1* and genotype analysis. (**A**) A diagram of the *mabp1* locus before and after homologous recombination of the targeting construct is shown. Exons 2 and 3 of *mabp1* were replaced by a neomycin resistance cassette in opposite transcriptional orientation. Black boxes indicate location of probes A, B, and C for Southern blot analysis (data not shown) and primers for genotyping the F2 generation by PCR analysis (**B**) performed on tail DNA of wt mice (lane 1), $mabp1^{-/-}$ mice (lane 2) and $mabp1^{+/-}$ mice (lane 3), respectively. H = *Hin*dIII, fragment sizes are indicated on the right in base pairs. (**C**) The expression of mAbp1 and actin as a control (upper and lower panel, respectively) is monitored in cleared cellular lysates from total brain (lanes 1–3) and spleen (lanes 4–6) of wt mice (lanes 1 and 4) and mutant mice harboring either one or two inactivated *mabp1* alleles (lanes 2, 5 and 3, 6, respectively) by immunoblot analysis. Relative molecular mass of marker proteins is indicated on the right in kDa.

 ©2006 European Molecular Biology Organization

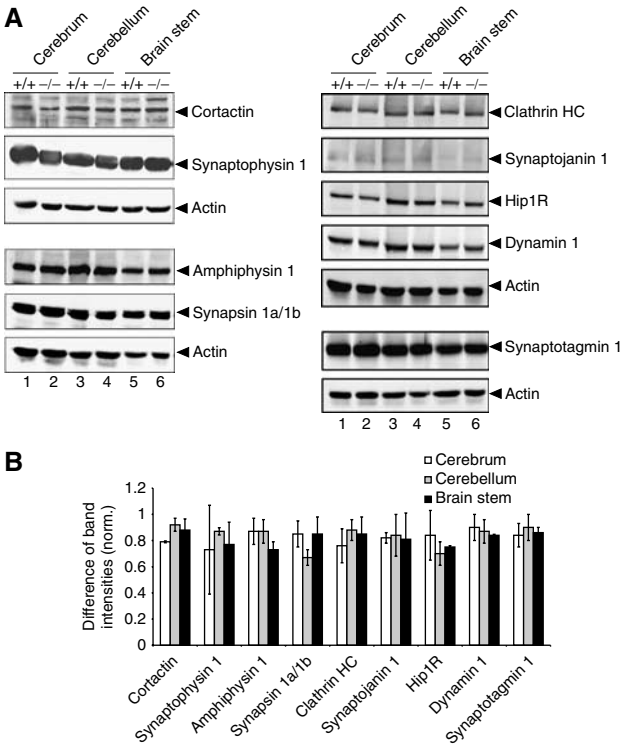

Figure 2 Loss of mAbp1 does not affect expression of functionally related proteins. (**A**) Expression levels of amphiphysin, synapsinIa/Ib, synaptotagmin1, clathrin HC, synaptojanin1, Hip1R, dynamin, cortactin, and synaptophysin were analyzed with specific antibodies in cerebrum (lanes 1 and 2), cerebellum (lanes 3 and 4) and brain stem (lanes 5 and 6). Actin levels were used as loading control. (**B**) Plotted is the difference between band intensities of the analyzed proteins in wt and *mabp1*$^{-/-}$ mice normalized to the corresponding band intensity of the wt level. Band intensities were quantified with Gel Pro-Analyzer software (INTAS, Göttingen, Germany) and normalized to actin. The diagram depicts relative differences between the expression levels of the analyzed proteins in *mabp1*$^{-/-}$ and wt mice. Error bars represent standard deviations calculated on the basis of two independent experiments.

into blastocysts of C57BL/6 mice. Male chimeras were bred with wild-type (wt) BALB/c females. PCR-based genotyping (Figures 1A and B) identified *mabp1*$^{+/+}$, *mabp1*$^{+/-}$, and *mabp1*$^{-/-}$ mice in the F2 generation with Mendelian ratios of 35, 41, and 24%, respectively ($n = 206$). *mabp1*-deficient mice are viable and both genders are fertile and equally represented in the total F2 population as well as in the *mabp1*$^{-/-}$ subpopulation. The absence of mAbp1 protein expression in *mabp1*$^{-/-}$ mice is shown for lysates from total brain and spleen in immunoblot analysis (Figure 1C). Note that in heterozygous animals, mAbp1 is expressed at a lower level than that in wt controls (lanes 3, 6 and 1, 4, respectively).

Expression level of proteins that are structurally and/or functionally related to mAbp1 is unaltered in mAbp1 mutant mice

As described, mAbp1 is a multidomain adaptor interacting with a variety of other proteins, especially in neuronal cells. We thus assessed whether loss of mAbp1 affects the expression levels of other proteins implicated in mAbp1 function. Figure 2 shows immunoblot analysis of cleared cellular lysates of cerebrum (lanes 1 and 2), cerebellum (lanes 3 and 4), and brain stem (lanes 5 and 6) with antibodies to amphiphysin, synapsinIa/Ib, synaptotagmin1, clathrin HC, synaptojanin1, Hip1R, dynamin, synaptophysin, and cortactin. Quantification of band intensities (Figure 2C) revealed no significant changes in the expression levels of these proteins in *mabp1*-deficient brain cells.

Pathological changes in mabp1-deficient mice

Total necropsy of *mabp1*$^{-/-}$ mice showed pathological changes in the spleen, heart, and lung. As shown in Figure 3A and Table I, splenomegaly was evident in 4–12 months aged *mabp1*$^{-/-}$ mice. Normalized spleen weights are increased approximately two-fold in female and male *mabp1*$^{-/-}$ mice (Table I). Increased spleen weights were consistently also

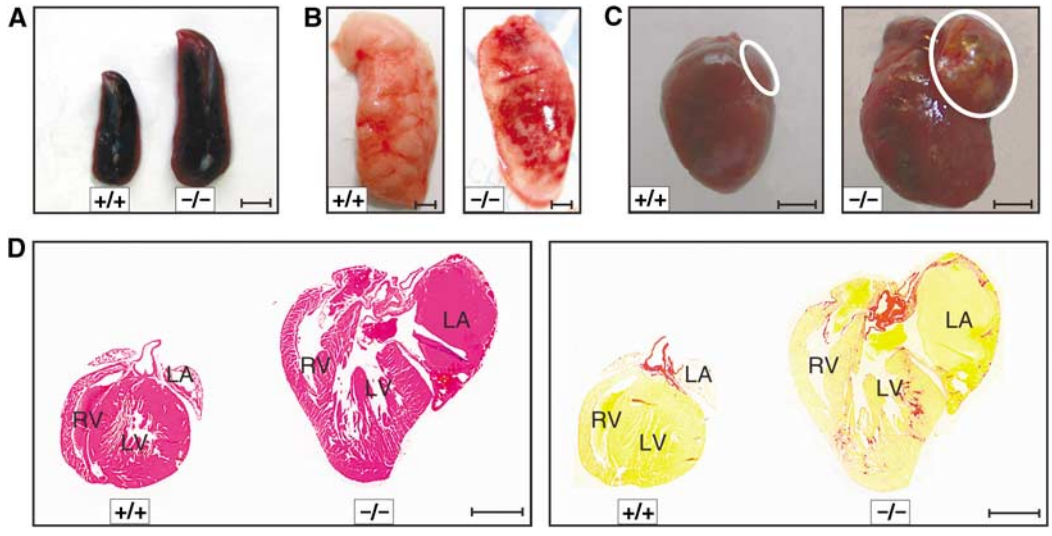

Figure 3 Altered anatomy of the spleen, lung, and heart in *mabp1*-deficient mice. (**A**) Splenomegaly was identified in *mabp1*$^{-/-}$ mice (scale bar 0.25 cm). (**B**) Abnormal structure is observed in lobes of *mabp1*$^{-/-}$ lung compared to that of wt control mice (scale bars 0.25 cm). (**C**) *mabp1*$^{-/-}$ mice possess an enlarged heart with an enormously enlarged left atrium (encircled, scale bars 0.25 cm). (**D**) Four chamber dilatations and a left atrial thrombus is observed in *mabp1*$^{-/-}$ mice (hematoxilin/eosin (HE) staining, left panel), additionally all chambers of the *mabp1*$^{-/-}$ heart show extensive fibrosis (red) (Sirius red staining, right panel). For comparison, an age-matched wt heart is shown. RV = right ventricle; LV = left ventricle; and LA = left atrium (scale bars 2 mm).

©2006 European Molecular Biology Organization

observed in heterozygous *mabp1*$^{+/-}$ mice indicating a gene dosage effect. Loss of mAbp1 leads to heart failure symptoms (observed in 44.7 and 48.1% of *mabp1*$^{-/-}$ and *mabp1*$^{+/-}$ male mice and in 48.9 and 33.3% of *mabp1*$^{-/-}$ and *mabp1*$^{+/-}$ female mice, respectively) with labored breathing and generalized edemia (Figures 3B and C). *mabp1*-deficient hearts show dilation of all four chambers associated with thrombi in atrias and ventricles (Figure 3D, left panel) and massive interstitial fibrosis (Figure 3D, right panel). Lungs of *mabp1*$^{-/-}$ mice possess abnormal structure and develop emphysema and edemia (Figure 3B), which are frequently associated with heart insufficiencies, and hence may represent a secondary mAbp1 deficiency symptom. The data show that mAbp1 expression is required for proper function of different tissues in a gene dosage-dependent manner.

Receptor-mediated endocytosis is slightly reduced in mabp1-deficient mice

As mAbp1 has been implicated in vesicle endocytosis and trafficking (Kessels *et al*, 2001; Mise-Omata *et al*, 2003), we investigated transferrin uptake in fibroblasts from day 15 *mabp1*$^{+/+}$ and *mabp1*$^{-/-}$ embryos. Following incubation of mouse embryonic fibroblasts (MEFs) with Cy2-conjugated mouse transferrin, only minor differences in transferrin internalization were observed (Figure 4A). The amount of transferrin uptake was measured at different time points by quantitative analysis of the per-cell fluorescence intensities. Comparison of the initial internalization rates revealed a modest decrease (~20%) in transferrin uptake in *mabp1*-deficient fibroblasts (Figure 4B). It thus appears that loss of mAbp1 can be partially compensated by other proteins or that mAbp1 functions in a step downstream of vesicle budding and fission.

The functional recycling pool size is reduced in mabp1-deficient hippocampal neurons

Clathrin-mediated endocytosis (CME) plays a fundamental role in presynaptic exo–endocytic vesicle cycling. Thus, we performed live cell imaging on hippocampal neurons derived from *mabp1*$^{-/-}$ and *mabp1*$^{+/+}$ mice using the fluorescent tracer FM1–43 to directly assess exo–endocytoic turnover of synaptic vesicles (Betz and Bewick, 1992; Ryan and Smith, 1995). Images of FM-dye-stained hippocampal neurons from wt and *mabp1*-deficient mice do not show any obvious differences in arborization, bouton density, or distribution (Figure 5A). Upon staining by triggering action potentials (APs) and dye washout FM-labelled boutons were maximally unloaded with 900 APs. Differences between the fluorescence signals (ΔF) before and after complete destaining yield a measure of the relative numbers of endocytosed and recycled vesicles. In Figure 5B, ΔF values of individual boutons for a 40-AP loading train are plotted in a histogram for both phenotypes. This stimulus is expected to release most vesicles docked at the AZ, belonging to the readily releasable pool (Stevens and Williams, 2000). The average ΔF value is significantly smaller in *mabp1*-deficient boutons, indicating that the recycled vesicles repopulate the readily releasable pool less efficiently in *mabp1*$^{-/-}$ synapses. As shown in

Table I Increased relative spleen weights in *mabp1*$^{+/-}$ and *mabp1*$^{-/-}$ mice

Gender[a]	Genotype[a]	Spleen ($10^{-3} \times$ g)/body (g)[b]	
Female	+/+	4.39±0.32	
	+/−	5.52±1.02	0.023*
	−/−	9.06±3.49	0.011*
Male	+/+	3.47±0.24	
	+/−	6.41±2.66	0.082
	−/−	6.89±2.92	0.016*

[a]$n = 15$ for each gender and genotype (*mabp1*$^{+/+}$, *mabp1*$^{+/-}$, *mabp1*$^{-/-}$); 4–12 months aged mice were analyzed.
[b]Weights of spleens ($10^{-3} \times$ g) including standard deviations were normalized to the bodyweight (g) of mice. A significant difference is noted with an asterisk ($P < 0.05$).

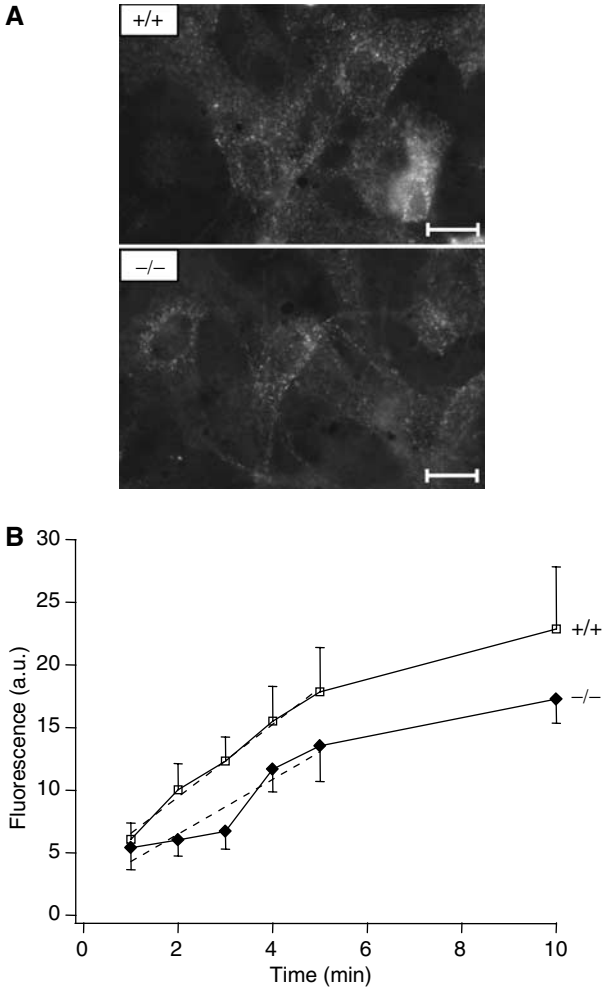

Figure 4 Receptor-mediated endocytosis is slightly reduced in *mabp1*-deficient mice. (**A**) Representative fluorescence images of *mabp1*$^{+/+}$ and *mabp1*$^{-/-}$ MEFs show the uptake and internalization of Cy2-labelled transferrin (10 min incubation; scale bars 1.45 μm). (**B**) Mean fluorescence intensities of single MEFs after incubation with Cy2-labelled mouse transferrin for 1–5 and 10 min at 37°C (errors in s.e.m.; $n = 69, 45, 49, 45, 62, 42$ for $t = 1, 2, 3, 4, 5, 10$ min for *mabp1*$^{+/+}$ and $n = 43, 74, 57, 37, 26, 28$ for *mabp1*$^{-/-}$, respectively). Initial internalization rates were determined by regression analysis (dashed lines) over the first 5 time points (slopes of 2.9±0.16 for *mabp1*$^{+/+}$ cells and 2.2±0.45 for *mabp1*$^{-/-}$ cells, respectively) revealing a moderate reduction of approximately 20% of receptor-mediated endocytosis in *mabp1*-deficient cells (errors of slopes are the confidence intervals at 95% level).

©2006 European Molecular Biology Organization

Figure 5C, this average ΔF value rises with increasing stimulus length until reaching a plateau for about 600 APs in control (*mabp1*$^{+/+}$) synaptic boutons, in agreement with published data (Ryan *et al*, 1996; Kim *et al*, 2002). FM1–43 uptake in *mabp1*$^{-/-}$ boutons also plateaued at about 600 APs, but ΔF, that is, the size of total recycling pool, is reduced to the same degree as the recycling to the readily releasable pool.

We next compared the destaining kinetics of presynaptic terminals loaded with FM1–43 to saturation (Figure 5D). During brief electrical stimulation (40 AP at 20 Hz), both *mabp1*$^{+/+}$ and *mabp1*$^{-/-}$ boutons released about 20% of dye. The remaining dye fraction was released by prolonged stimulation (900 APs) with the same kinetics in both *mabp1*$^{+/+}$ and *mabp1*$^{-/-}$ boutons. These data indicate that in *mabp1*-deficient neurons, recycled synaptic vesicles undergo exocytosis with the same release probability as in *mabp1*$^{+/+}$ control cells, but the size of the functional total recycling vesicle pool is somewhat reduced. Taken together, styryl dye uptake probing stimulated endocytosis in hippocampal boutons is reduced to a similar degree as receptor-mediated endocytosis in MEFs probed by transferrin uptake. Thus, mAbp1 may be more important in a subsequent step, that is, in the proper recycling of synaptic vesicles.

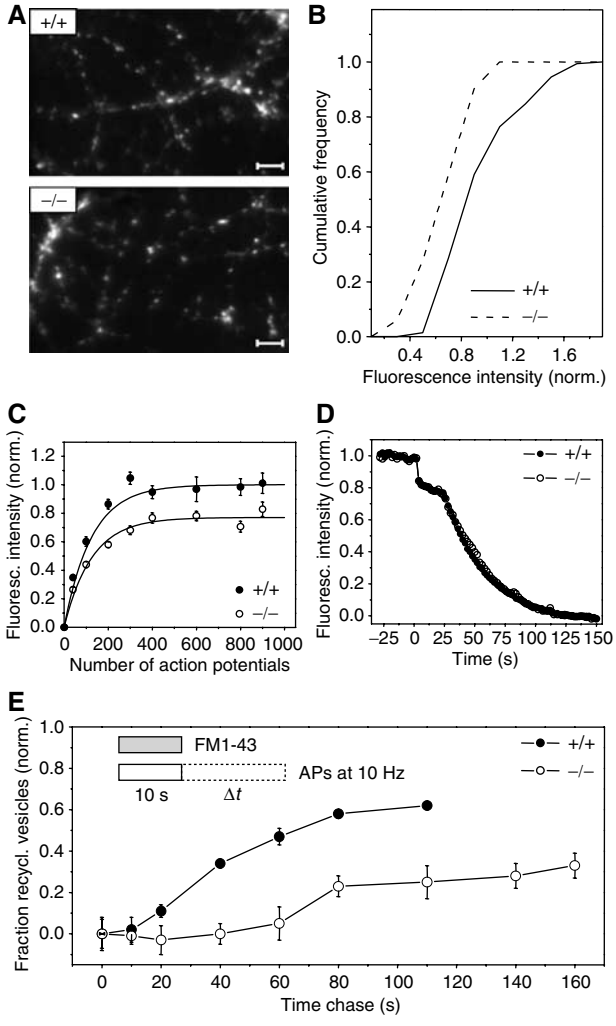

The reformation of fusion-competent synaptic vesicles is severely impaired and delayed in mabp1-deficient boutons

To test a potential role of *mabp1* in synaptic vesicle recycling or repriming, we performed pulse-chase experiments. Boutons were labelled during a 10 s pulse of FM1–43 with 100 APs at 10 Hz (Figure 5E, inset, for details see Materials and methods). Electrical field stimulation was continued after the FM-dye pulse for different chase times (0–160 s). Vesicles endocytosed during dye application recycle back to the releasable pool, are reprimed, and eventually exocytosed for a second time, thereby releasing their trapped FM dye. The residual fraction of labelled vesicles for a given chase time Δt was determined as the ΔF value for complete destaining 10 min later. Plotting the fractions of recycled vesicles (see figure legend for details) for each chase time revealed a severe defect in the regeneration of functional synaptic vesicles during prolonged stimulation (Figure 5E). For control *mabp1*$^{+/+}$ boutons, repriming kinetics and efficacy were similar to those previously described for rat hippocampal neurons (Ryan and Smith, 1995). The minimum repriming time was about 15 s, and about 60% of the dye taken up is released during 100 s of continued stimulation. In contrast, in *mabp1*$^{-/-}$ synapses the minimum repriming time was delayed four-fold to 60 s, and only about 30% of the dye could be released again during stimulation continued for up to 150 s. These results reveal a dramatic defect in the reformation of functional synaptic vesicles in the absence of *mabp1*, indicating that mAbp1 acts downstream of vesicle budding.

Figure 5 Synaptic vesicle recycling in hippocampal synapses of *mabp1*-deficient mice is severely impaired. (**A**) Exemplar images of FM1–43-stained axonal processes of cultured hippocampal neurons derived from wt and *mabp1*$^{-/-}$ mice. No obvious differences in arborization, bouton density, or distribution can be seen (scale bar 3.2 μm). (**B**) Cumulative distribution of vesicle turnover during a loading train of 40 APs, measured by FM1–43 at $n(3) = 144$ and $n(2) = 51$ individual synaptic boutons for *mabp1*$^{+/+}$ and *mabp1*$^{-/-}$, respectively. Fluorescence intensities are normalized to the average FM fluorescence of *mabp1*$^{+/+}$ boutons. The mean value of the distribution for *mabp1*$^{-/-}$ neurons is 0.75 ± 0.03 (s.e.m.). (**C**) Size of the functional synaptic vesicle pool in dependence of stimulus length for *mabp1*$^{-/-}$ (open circles) and *mabp1*$^{+/+}$ boutons (filled circles). Boutons were loaded by different AP numbers and fully destained with 900 APs at 10 Hz. Error bars are confidence intervals of the mean at 95% level. Numbers of experiments were $n = 3, 4, 5, 2, 4, 2, 3, 3$ for *mabp1*$^{+/+}$ and $n = 2, 4, 6, 2, 4, 4, 2, 4$ for *mabp1*$^{-/-}$ neurons, respectively, each comprising typically 50–100 individual boutons. The total recycling pool size estimated from a single exponential fit (solid lines) for *mabp1*$^{-/-}$ is 0.77 ± 0.02 (s.d.) of that determined from a fit for *mabp1*$^{+/+}$ (1 ± 0.02 (s.d.)). (**D**) Average FM1–43 release kinetics of maximally loaded (900 APs at 10 Hz) synaptic boutons for two consecutive destaining stimuli (40 AP at 20 Hz and 900 AP at 10 Hz) are similar for *mabp1*$^{+/+}$ and *mabp1*$^{-/-}$ neurons. Data are normalized to fluorescence signals before destaining after subtraction of nonreleasable background. (**E**) Repriming kinetics determined by FM1–43 pulse-chase experiments. Plotted is the fraction of dye released during a given chase time Δt normalized to the maximum upload ΔF_0 for chase time $\Delta t = 0$, that is, $(\Delta F_0 - \Delta F_{\Delta t})/\Delta F_0$. Under prolonged stimulation, reformation of fusion-competent vesicles is severely impaired and delayed. The minimum repriming time of 10–20 s for control *mabp1*$^{+/+}$ is delayed to 60–80 s in *mabp1*$^{-/-}$ synapses. After 100 s, only 25 versus 60% of retrieved membrane is releasable again in *mabp1*$^{-/-}$ synapses. Numbers of experiments were $n = 4, 3, 3, 3, 2, 2, 2$ for *mabp1*$^{+/+}$ and $n = 5, 4, 4, 4, 3, 3, 2, 2, 2$ for *mabp1*$^{-/-}$ neurons, respectively, each comprising typically 50–100 individual boutons. Error bars are confidence intervals of the mean at 95% level.

©2006 European Molecular Biology Organization

Ultrastructural analysis reveals three-fold more endosome-like intermediates in mabp1-deficient boutons

To correlate the physiology of synaptic boutons with their ultrastructure, we analyzed wt and *mabp1*$^{-/-}$ synapses in hippocampal cultures with respect to total numbers of vesicles and the number of vesicles docked to the AZ by electron microscopy (Figure 6). The numbers of synaptic vesicle profiles per synapse area (Figure 6B and C), closer than 20 nm to or docked at the AZ per AZ length (Figure 6D and E), were not significantly different. We observed, however, a significant accumulation of endosome-like structures (>60 nm), presumably endocytic intermediates, in *mabp1*$^{-/-}$ hippocampal boutons (Figure 6F). These cisternae may either represent true endosomal intermediates (Heuser and Reese, 1973) or, more likely, may arise from bulk endocytosis of large infoldings from the plasma membrane (Takei *et al*, 1996; Richards *et al*, 2000). The physiological and ultrastructural data reveal an important role for mAbp1 in CME of synaptic vesicle membrane. The severe delay in recycling observed in the FM experiments can now be explained on the ultrastructural level by a delay in vesicle fission either from the plasma membrane, leading to the formation of large infoldings, or from endosomal intermediates, resulting in the accumulation of endosome-like structures.

Synaptic localization of mAbp1-associated proteins is unaltered in mabp1-deficient mice

These physiological and ultrastructural data prompted us to ask whether synaptic expression and localization of mAbp1-associated proteins involved in CME may be altered. Thus, we determined synaptic expression and localization of clathrin light chain (CLC), dynamin1, and F-actin by immunocytochemistry. Synaptic boutons were identified by costaining

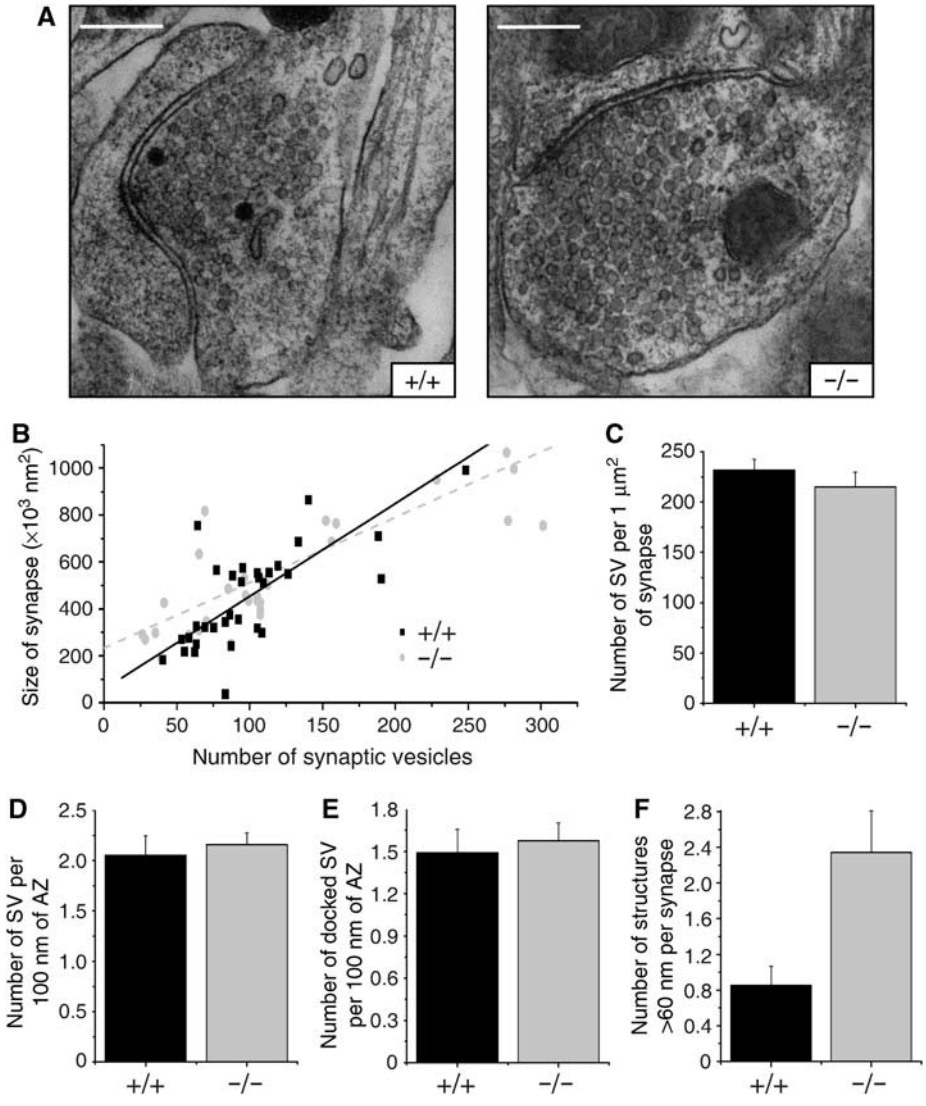

Figure 6 Ultrastructural analysis of synaptic boutons in hippocampal cultures. (**A**) Representative synaptic boutons from wt and *mabp1*-deficient hippocampal cultures (scale bars 0.3 µm). (**B**) The distributions of the number of vesicles per bouton area are similar in wt ($n=34$) and *mabp1*$^{-/-}$ synapses ($n=30$). Total numbers of vesicles are 3729 for wt and 3630 for *mabp1*$^{-/-}$ synapses. (**C**) Average number of synaptic vesicles (SV) per 1 µm^2 bouton area are similar in wt (231.63±10.92) and *mabp1*$^{-/-}$ synapses (214.83±14.87). (**D**) Average numbers of morphologically docked vesicles per AZ length are similar in mAbp1-positive ($n=20$) and mAbp1-negative synapses ($n=25$). (**E**) Average numbers of vesicles close to the AZ (<20 nm) per AZ length are similar in wt ($n=20$) and *mabp1*$^{-/-}$ synapses ($n=25$). (**F**) The number of endosome-like intermediates per synapse is significantly higher in *mabp1*-deficient (2.497±0.464) than in wt (0.853±0.212) synapses.

 ©2006 European Molecular Biology Organization

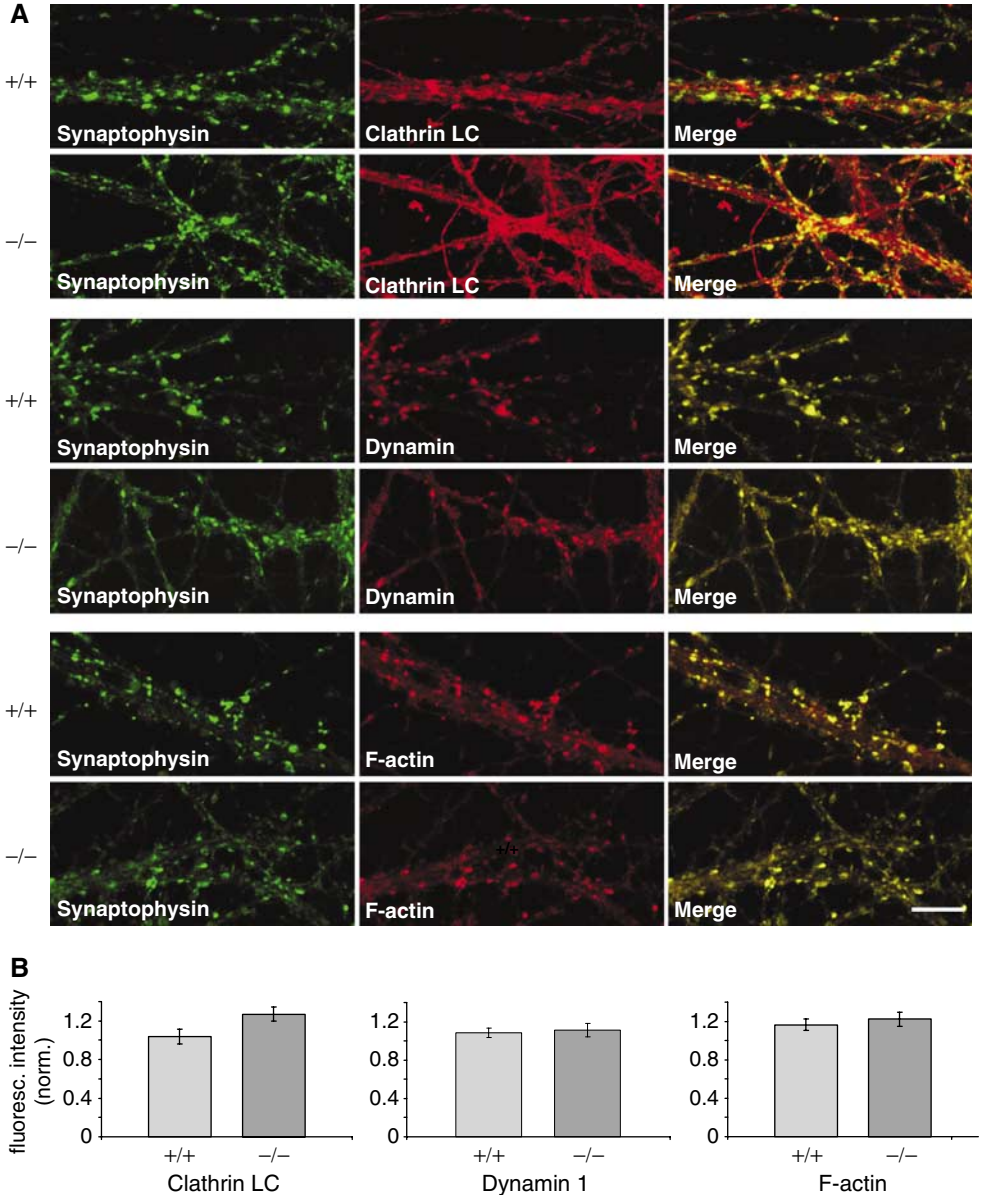

Figure 7 Localization of F-actin, dynamin1 and CLC in *mabp1*-deficient and wt hippocampal neurons. (**A**) Hippocampal neurons at 12–14 days *in vitro* (DIV) were stained with anti-dynamin1 and anti-CLC antibodies as well as with phalloidin together with anti-synaptophysin1 and imaged by laser scanning confocal microscopy (scale bar 10 μm). (**B**) Quantification of CLC, dynamin1, and F-actin expression in synaptophysin-positive puncta. Diagrams showing mean values of fluorescence intensities with s.e.m. normalized to synaptophysin1 fluorescence intensities.

for the *bona fide* synaptic marker protein synaptophysin1 (Figure 7A). The localization and distribution of synaptophysin1 is almost identical between hippocampal neurons of $mabp1^{+/+}$ and $mabp1^{-/-}$ mice (Figure 7A, left panels). Consistent with previous reports, we found extensive colocalization of synaptophysin1 with CLC, dynamin1, and F-actin in both $mabp1^{+/+}$ and $mabp1^{-/-}$ hippocampal neurons (Figure 7A, middle and right panels). Furthermore, we estimated the synaptic concentrations of CLC, dynamin1, and F-actin by quantifying fluorescence intensities in synaptophysin1-positive puncta only. These were identified and delimited in a user-unbiased manner by an automated detection algorithm (see Materials and methods for details). Averaged fluorescence intensities from different dishes analyzed on different days were normalized to the simultaneously recorded synaptophysin1 fluorescence intensities (Figure 7B), as these were identical in $mabp1^{-/-}$ and wt synapses. Although synaptic expression and localization of dynamin1 and F-actin were identical, CLC may be slightly enriched in *mabp1*-deficient boutons.

Profiling specific motor skills of mabp1 mutant mice

The observed presynaptic defect in mAbp1-negative neurons is associated with severe neuromotoric deficits of $mabp1^{-/-}$ mice. Between 60 and 290 days after birth, 64% of male and 54% of female $mabp1^{-/-}$ mice developed characteristic symptoms like ruffled up fur, muscle trembling, convulsions, partial paralysis of the hind limbs, and reduced body weight (Figure 8B and Supplementary Figure 1A and B). Hetero-

©2006 European Molecular Biology Organization

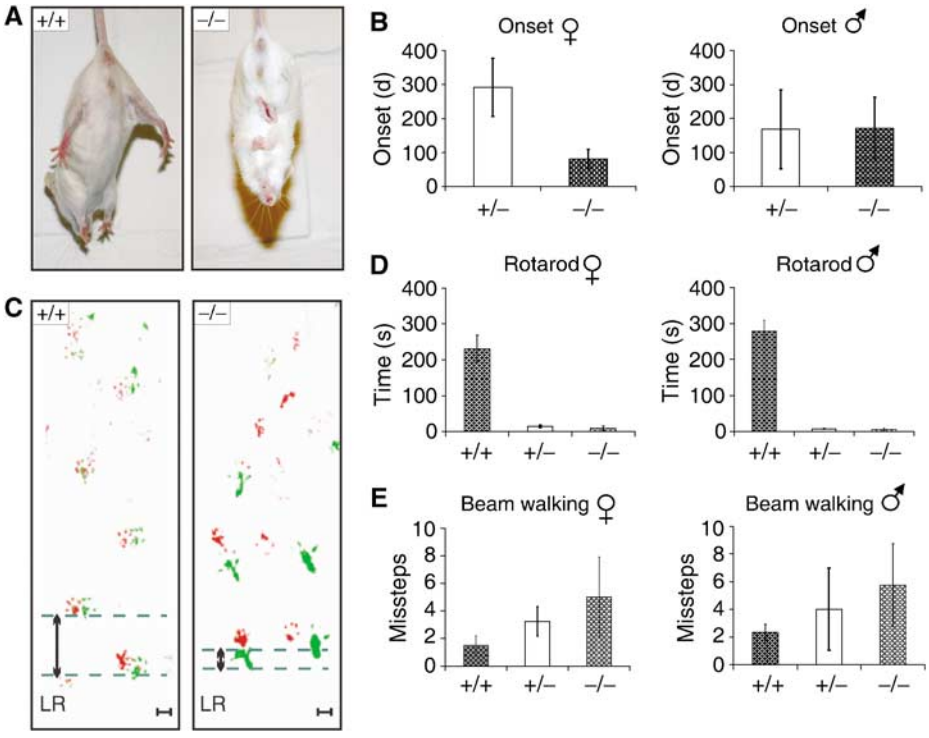

Figure 8 Characterization of behavioral abnormalities of *mabp1*$^{-/-}$ mice. (**A**) wt mice spread their limbs during a tail-suspension test while *mabp1*$^{-/-}$ mice react with hind- and forelimb clasping. (**B**) The onset of mAbp1 deficiency symptoms for female *mabp1*$^{+/-}$ ($n=16$) and *mabp1*$^{-/-}$ ($n=29$) mice as well as male *mabp1*$^{+/-}$ ($n=21$) and *mabp1*$^{-/-}$ ($n=24$) mice were investigated over a period of 1 year. No symptoms were identified for *mabp1*$^{+/+}$ littermates used as controls (female $n=12$, male $n=10$). Error bars represent standard deviations. (**C**) Evaluation of foot placement was performed by recording footprints of mice with differently painted forelimb (red) and hindlimb (green). Analysis of path geometry revealed differences in left–right (LR) alteration between *mabp1*$^{-/-}$ ($n=13$) and *mabp1*$^{+/+}$ mice ($n=9$) upon the onset of the disease symptoms (scale bar 1 cm). (**D**) In a Rotarod test, time to fall off (s) was determined in five test sessions performed every second day at a fixed daytime. A maximum score of 300 s was given to those mice not falling off within this period of time. The average time to fall off is shown with standard deviations. Female *mabp1*$^{+/+}$ ($n=2$), *mabp1*$^{+/-}$ ($n=3$), and *mabp1*$^{-/-}$ ($n=3$) mice as well as male *mabp1*$^{+/+}$ ($n=2$), *mabp1*$^{+/-}$ ($n=3$), and *mabp1*$^{-/-}$ ($n=4$) mice with no obvious mAbp1 deficiency symptoms were employed. (**E**) Beam walking experiments, performed three times at intervals of 1 week, revealed deficits in motor abilities in a gene dose-dependent manner. The average number of missteps was determined for female *mabp1*$^{+/+}$ ($n=4$), *mabp1*$^{+/-}$ ($n=6$), and *mabp1*$^{-/-}$ ($n=4$) mice and male *mabp1*$^{+/+}$ ($n=4$), *mabp1*$^{+/-}$ ($n=4$), and *mabp1*$^{-/-}$ ($n=5$) mice with no obvious symptoms. Error bars represent standard deviations.

zygous *mabp1*$^{+/-}$ mice also become affected, albeit at a lower frequency; that is, 44% of male and 19% of female *mabp1*$^{+/-}$ mice develop the described symptoms. Impaired locomotion and bad coordination are obvious from a tail-suspension test (Figure 8A). The average age at the onset of the neuromotoric malfunction is dependent on the gender. Female *mabp1*$^{-/-}$ mice acquire behavioral abnormalities earlier than their male counterparts (80 versus 170 days), but are less sensitive to loss of a single *mabp1* allele (Figure 8B). To test higher brain function and spatial learning, we aimed at applying the Morris water maze test (Morris, 1989). However, the ability to swim was severely and progressively affected in mutant mice (Supplementary Movies 1A and B) to such an extent that this test could not be conducted. Motoric behavioral capabilities were tested by Rotarod test, footprint analysis, and Beam walking.

Walking on a Rotarod is a difficult motor coordination and balance control test. *mabp1*$^{+/+}$ female and male mice maintained balance for 230 ± 36 and 278 ± 31 s, respectively (Figure 8D). Female *mabp1*$^{+/-}$ and *mabp1*$^{-/-}$ mice stayed on the Rotarod for 14 ± 4 and 9 ± 7 s. Male *mabp1*$^{+/-}$ and *mabp1*$^{-/-}$ mice persevered for 7 ± 1 and 5 ± 4 s, respectively. Severe deficits in motor performance are also obvious from altered foot placement investigated by gauging the trajectory of *mabp1*-deficient animals. A significant and progressive reduction in left–right alteration length of hind limbs became apparent in female and male *mabp1*$^{+/-}$ and *mabp1*$^{-/-}$ mice upon the onset of first symptoms (Figure 8C). In Beam walking experiments, wt mice reached the platform with approximately two missteps (Figure 8E). Male and female *mabp1*$^{+/-}$ and *mabp1*$^{-/-}$ mice made significantly more missteps in a gene dose-dependent manner (female *mabp1*$^{+/-}$ and *mabp1*$^{-/-}$ 4 and 6, respectively, and male *mabp1*$^{+/-}$ and *mabp1*$^{-/-}$ 3 and 5, respectively). The observed motoric dysfunctions are not caused by muscular defects as indicated by first, normal expression of acetylcholine receptor α-subunit, second unaltered muscle architecture (Supplementary Figure 2), and finally, normal grip strength of mAbp1-negative mice (data not shown). Collectively, our experiments demonstrate strongly reduced fine motor coordination of hetero- and homozygous *mabp1* mutant mice. Note that impaired Rotarod and Beam walking performances are observed before the appearance of any signs of illness or physical abnormalities. This shows that disturbed behavior is a direct consequence of the *mabp1* mutation and not an indirect result of loosing body weight or getting weaker.

©2006 European Molecular Biology Organization

Discussion

Previous studies implicated the cytoskeleton adaptor protein mAbp1 as a component of the endocytic machinery as it was found to bind several key molecules required for F-actin and membrane vesicle dynamics. The functional relevance of the reported protein–protein interactions, however, remained unclear. Here, we have analyzed the *in vivo* function of mAbp1 by gene targeting in mice. Our analysis of the resulting mouse mutants revealed a critical role of mAbp1 for the integrity of several organs, synaptic transmission, and normal neuromotoric function. Mechanistically, we could place mAbp1 function to a step orchestrating endocytic vesicle departure downstream of budding and fission from the plasma membrane.

Neonatal mAbp1 mutant mice develop without obvious pathological symptoms during the first weeks of life. About 4 months after birth, both homo- and heterozygous mAbp1 mutants develop severe organ abnormalities. The spleen size increases two- to four-fold. The exact reason for the splenomegaly is yet unclear, but an increased blood load containing the normal distribution of blood cell populations rather than histological alterations were routinely observed (data not shown). The hypertrophic heart of mAbp1 mutant mice is characterized by dilation of all chambers, which possess thrombi and massive interstitial fibrosis. Beside mAbp1, several actin-binding proteins, such as cardiac β-myosin heavy chain, cardiac actin, muscle LIM protein, lamin, or desmin, have been recently described to be critical for proper heart function (Seidman and Seidman, 2001). Mutations in these genes in mice or humans cause severe cardiomyopathies presumably owing to ineffective production or transmission of contractile forces, which renders affected hearts highly susceptible to mechanical stress. Presumably as a secondary effect, which is usually associated with heart failure, mAbp1 mutants develop emphysema and edemia also in the lung. These data show that *in vivo*, mAbp1 fulfills a nonredundant function, which is already compromised upon loss of a single *mabp1* allele and thus appears to be rate limiting.

To address mAbp1 function in more molecular details, we employed common experimental systems to study different stages of the endocytic process. We found a significant albeit moderate effect of mAbp1 ablation on transferrin and FM styryl dye uptake in embryonic fibroblasts and in synaptic boutons of primary hippocampal neurons, respectively. In line with these data, RNAi-mediated inhibition of mAbp1 expression (Mise-Omata *et al*, 2003) as well as overexpression experiments (Kessels *et al*, 2001; Mise-Omata *et al*, 2003) previously suggested an endocytic function of mAbp1 in mammalian cells including T-lymphocytes. The development and function of T cells is, however, almost normal in mAbp1-negative mice (Han *et al*, 2005; own unpublished results), indicating that a certain degree of redundancy exists at least in this cell type. Indeed, in yeast cells, the Sla2 protein is capable of compensating for the loss of Abp1 as endocytic defects are obvious only upon simultaneous loss of both proteins (Holtzman *et al*, 1993; Yang *et al*, 1999). In support of this, lack of the mammalian Sla2 ortholog, Hip1R, does not affect growth and viability of genetically engineered mouse mutants (Hyun *et al*, 2004). Our data do not argue against the possibility that the presence of mAbp1 may compensate for the loss of Hip1R in these mice, but definitely exclude a functional replacement of mAbp1 by Hip1R. Nonetheless, the two proteins may function in a common step of the endocytic process, but our live cell imaging data of the repriming kinetics in *mabp1*-deficient boutons establishes that the major and specific function of mAbp1 is downstream of clathrin vesicle formation at the stage of vesicle fission. This is also supported by the ultrastructural analysis showing an accumulation of endosome-like endocytic intermediates in *mabp1*-deficient cells. In support of this and as shown more recently, association of mAbp1 with actin comet tails occurs subsequently to dynamin function and clathrin release (Merrifield *et al*, 2005; Newpher *et al*, 2005; Yarar *et al*, 2005).

The presynaptic mAbp1 function can apparently not be compensated for by other endocytic proteins. mAbp1 is instrumental for normal neuromotoric function as indicated by the severely and progressively disturbed motor skills accompanied with mAbp1 deficiency symptoms. The importance of mAbp1 for neuronal function fits with previous reports demonstrating colocalization and linkage of mAbp1 with various neuronal proteins such as piccolo, ProSAP1 and ProSAP2 (Fenster *et al*, 2003; Qualmann *et al*, 2004), synaptojanin1, synapsin1, dynamin1 (Kessels *et al*, 2001), and Rvs167p/amphiphysin (Lila and Drubin, 1997). Lack of three of the latter four proteins reduces the total pool of recycling vesicles to approx. 60–70% (Ryan *et al*, 1996; Di Paolo *et al*, 2002; Kim *et al*, 2002). A four-fold increase in vesicle repriming time is observed in synaptojanin1 (Kim *et al*, 2002) as well as in our *mabp1*-deficient cells, which limits the availability of fusion-competent vesicles and should result in synaptic depression in highly active neurons. This explains the motoric dysfunctioning. Surprisingly, no abnormalities on the overall morphology of the CNS were observed by various histological stainings of brain and spinal cord sections of mAbp1-mutant mice (data not shown).

In conclusion, gene targeting in ES cells has elucidated a central and nonredundant *in vivo* function of the cytoskeleton adaptor protein mAbp1 for endocytic membrane transport. Secondly, mAbp1 acts predominantly and in a rate-limiting manner downstream of clathrin vesicle formation (and Hip1R function) at a stage of vesicle fission and transport. In the absence of mAbp1 expression, several cell types become affected, most notably neurons with respect to synaptic transmission, causing severe behavioral abnormalities. This provides further and direct evidence for the importance of the actin cytoskeleton and its inducible reorganization by actin-binding proteins in endocytic processes and vesicle trafficking (Benesch *et al*, 2005; Merrifield *et al*, 2005; Yarar *et al*, 2005). In future studies, mAbp1 mouse mutants may serve as a model system to investigate human diseases such as cardiac hypertrophy or neuronal disorders.

Materials and methods

Construction of targeting constructs

Genomic DNA encompassing parts of intron 1 and intron 3 to exon 10 were amplified by PCR and cloned into pCRII-TOPO vector (Invitrogen, Karlsruhe, Germany). A 822 bp *Sal*I/*Eag*I fragment was replaced by a 1100 bp *Eag*I/*Xho*I neomycin resistance cassette fragment from pBSmuneopac (kindly provided by S Kuppig, Freiburg) to create the final targeting *abp1*KO vector having the neomycin resistance cassette in place of exons 2 and 3 and in reverse transcriptional orientation of the *abp1* gene.

©2006 European Molecular Biology Organization

Screening of ES cells

BALB/c ES cells selected with G418 for the uptake of *Pvu*I-linearized targeting vector were screened for correct homologous recombination by Southern blot analysis using three different hybridization probes. A 5′ external probe (probe A: 299 bp, parts of exon 1 and adjacent sequence of intron 1) detected homologous recombination of the short arm, probe B of the neomycin resistance cassette (probe B: 435 bp, neomycin resistance cassette specific) monitored single insertion of the targeting construct, and probe C (probe C: 306 bp, encompassing exons 7 and 8) served as a 3′ internal probe.

Genotyping

Tail biopsies were incubated with 3 U (0.3 μg/μl) of Proteinase K (Promega, Mannheim, Germany) in 300 μl lysis buffer (10 mM Tris, pH 8.0, 50 mM KCl, 0.45% Tween 20, 0.45% NP40) overnight with agitation at 55°C. Subsequent incubation at 95°C for 10 min inactivated Proteinase K. Samples were centrifuged for 30 s and directly used for PCR analysis with the Taq PCR Master Mix Kit (Qiagen, Hilden, Germany). PCR primers 5′CACTGTTCATCTGCCCC AGCAGC3′ and 5′GGCTCTATGGCTTCTGAGGCGGA3′ were used to generate a 1138 bp fragment of the inactivated *mabp1* alleles and primers 5′CTGCTGTCTACCCTCAGGCTATG3′ and 5′GCCAGCCACAC GGATGTCATTGC3′ to generate a 611 bp amplicon of the wt allele, respectively.

Immunoblotting of mouse tissue proteins

Mouse tissues (100 mg) were homogenized in 100 μl 1 M Tris–HCl, pH 6.8, in an ultraturrax and supplemented with 500 μl loading buffer (62.5 mM Tris–HCl, pH 6.8, 20 mM DTT, 20% glycerol, 6% SDS, 0.02% bromophenol blue). Samples were agitated for 10 min, heated to 95°C for 5 min, and centrifuged for 10 min at 7000 *g*. Equal amounts of protein supernatants were analyzed by specific antibodies.

Monitoring specific motor skills

Tail-suspension test. Mice were suspended in the air by the tail for 20–60 s to verify clasping behavior. *Rotarod test*. Mice were trained on the Rotarod (TSE Scientific Systems, Bad Homburg, Germany) at a constant rotation speed of 26 r.p.m., to ensure that wt mice were capable of running the test without getting tired and unconcentrated. The time to fall off of the Rotarod was measured. *Footprint test*. Feet were painted with nontoxic paints and placed in a 50 cm long, 10 cm wide, 10 cm high runway with an inciting enclosed box to hide at the end. *Beam walking*. Mice had to cross a 50 cm long strip of wood with a diameter of 1 cm to reach an attached escape box. The number of missteps was counted.

Histological studies and mouse cell culture

Paraformaldehyde-fixed LV tissue slices were embedded and stained as described (Hilfiker-Kleiner *et al*, 2004). Primary MEFs were isolated from embryos at day 15 of gestation. Cells were grown in Dulbecco's modified Eagle's medium (DMEM) containing 15% fetal calf serum, penicillin/streptomycin, nonessential amino acids, glutamax, and β-mercaptoethanol in a 37°C incubator with 5% CO_2. Hippocampal neurons from regions CA1–CA3 of 1-day-old *mabp1*$^{-/-}$ and *mabp1*$^{+/+}$ mice were cultured and maintained as described (Klingauf *et al*, 1998).

Statistical analysis

Data were analyzed using the program STATISTICA 6.0. Weights of spleens were normalized to the body weight; mean values and standard deviation were calculated and examined for normal distribution by Smirnov–Kolmogorov test of normality. Subsequently, a one-way analysis of variance was used to determine the levels of difference between all groups/genotypes. The *P*-value for significance was set to 0.05.

Transferrin uptake assay

MEFs, grown to 50–60% confluency, were incubated for 2 h at 37°C in starving medium (serum-free DMEM containing 20 mM HEPES and 0.1% BSA). Cells were then incubated on ice for 5 min and loaded with Cy2-labelled mouse transferrin (20 μg/ml; Dianova, Hamburg, Germany) for 15 min at 4°C. Transferrin internalization was triggered by raising the temperature to 37°C for 1–5 and 10 min. Cells were washed with ice-cold starving medium and PBS containing 10 mM $MgCl_2$ immediately thereafter, followed by two wash steps with 0.2 M sodium acetate (pH 4.5) and 0.5 M NaCl to remove surface-bound transferrin. Before fixation with 4% paraformaldehyde, cells were washed two times with cold starving medium and once with PBS. Images were taken with a slow-scan CCD camera (Sensicam QE, PCO, Kelheim, Germany) using a × 63/1.2NA W objective on an inverted microscope (Axiovert 135 TV, Zeiss, Oberkochen, Germany). Single-cell fluorescence intensities were determined by subtraction of background and autofluorescence of nonstained control cells (mock treatment) for all time points.

Quantitative FM1–43 imaging and analysis

Neurons grown on coverslips were mounted in a laminar flow perfusion chamber and imaged with an ICCD camera (PentaMAX, Princeton Instruments, Monmouth Junction, USA) through a × 63/1.2W objective on an inverted microscope (Axiovert S100, Zeiss, Oberkochen, Germany) using a monochromator for excitation at 470 nm (Polychrome IV, TILL Photonics, 10 nm bandwidth), and dichroic and emission filters 495DCLP and HQ560/40, respectively (AHF Analysetechnik, Tubingen, Germany). Cells were perfused with a modified Tyrode's solution containing 150 mM NaCl, 5 mM KCl, 2 mM $CaCl_2$, 1 mM $MgCl_2$, 10 mM HEPES, and 30 mM glucose (330 mOsm, pH 7.3). For electric field stimulation (1 ms pulses, 40 mA, delivered by platinum–iridium electrodes spaced at 15 mm), 10 μM 6-cyano-7-nitroquinoxaline-2,3-dione and 50 μM D,L-2-amino-5-phosphonovaleric acid were added to prevent recurrent activity. FM1–43 (Molecular Probes Inc., Eugene, OR) was used at a concentration of 10 and 15 μM for global and local application, respectively, left in the bath for one more minute after the end of stimulation, and then washed off for 10 min. For rapid local perfusion, an SF77 fast step perfusion system was utilized (Warner Instruments, USA). Fluorescence intensities of individual synapses were quantified by averaging a 4 × 4 pixel area centered at the fluorescent punctum.

Electron microscopy

Primary cultures of hippocampal neurons were prepared from wt and *mabp1*$^{-/-}$ mice at postnatal days 0–1 as described previously. On 12–14 days, *in vitro* cells were fixed overnight at 4°C in cacodylat buffer containing 2.5% glutaraldehyde, 1% paraformaldehyde, and 0.1% tannic acid. After three washes in cacodylat buffer, cells were postfixed with 1% osmium tetroxide at room temperature (RT) for 1 h, extensively washed with deionized distilled water, and stained with 1.5% uranyl acetate. Cultures were then embedded in Epon 812 after dehydration in an ethanol series. Ultrathin sections (~60 nm) were collected on Formvar-coated nickel grids, stained with uranyl acetate (7 min) and lead citrate (2 min), and viewed with a Zeiss EM912 electron microscope, photographed, and printed at a final magnification of × 50 000. Morphological analysis was performed with Metamorph software (Molecular Devices, Downingtown, PA).

Immunocytochemistry and data analysis

Hippocampal cells were fixed with 4% paraformaldehyde after 12–14 days of culture, permeabilized, and blocked simultaneously in PBS with 0.4% Saponin and 2% normal goat serum for 1 h and incubated with primary antibodies specific for synaptophysin1, dynamin1, and CLC for 16 h at 4°C. Alexa Fluor 488-conjugated goat anti-rabbit (Molecular Probes; MoBiTec, Göttingen, Germany) and Cy3-conjugated goat anti-mouse (Dianova, Hamburg, Germany) antibodies were used as secondary antibodies. F-actin staining was performed with phalloidin–TRITC (Sigma-Aldrich, Munich, Germany) concomitantly with secondary antibody incubation for 1 h at RT. Cells were mounted in Citiflour AF1 (Science Services, Munich, Germany) and fluorescence images were captured simultaneously by confocal laser scanning microscopy (Leica SP2, × 63/1.2W objective, laser beam expanded to fill back pupil of objective, 59 nm pixel size, pinhole set to 1 Airy). Images were background subtracted and further analyzed by self-written macros in Igor Pro (Wavemetrics, Lake Oswego, OR, USA). To avoid the bias introduced by manual selection of synaptophysin1-marked boutons, an automated detection algorithm was used. Fluorescence images stained for synaptophysin1 were subjected to an *à-trous* wavelet transformation with the level $k = 4$ and detection level $l_d = 1.0$ (Olivo-Marin, 2002), resulting in a segmented mask image. Spots on mask images, each representing putative functional boutons, were identified, and only masks with areas between 4 and 20 pixels were accepted for calculating bouton fluorescence intensities in all simultaneously recorded fluorescence images.

©2006 European Molecular Biology Organization

Antibodies

Polyclonal anti-SH3P7 antibody (88-B2) and monoclonal anti-synapsinIa, Ib were described previously (Larbolette *et al*, 1999; Giovedi *et al*, 2004). The anti-dynamin antibody, anti-clathrin heavy-chain antibody, and the anti-Hip1R antibody were purchased from BD Bioscience (Heidelberg, Germany) and the anti-synaptojanin1 antibody from Synaptic Systems (Göttingen, Germany). The anti-actin antibody, anti-CLC antibody (Clone Con. 1), and the anti-cortactin antibody (KE-20) were from Sigma Aldrich (Munich, Germany). Anti-amphiphysin, anti-synaptotagmin, and anti-synaptophysin antibodies were kindly provided by R Jahn (MPI for Biophysical Chemistry, Göttingen, Germany). Secondary antibodies were purchased from Perbio/Pierce (Bonn, Germany).

Supplementary data

Supplementary data are available at *The EMBO Journal* Online.

Acknowledgements

We thank Benoit Kanzler (Transgenic Unit, MPI Freiburg) for generating chimeric mice by ES cell injection, Harald Jockusch for supporting analysis of skeletal muscle, and Marion Knufinke for caring and breeding of mice. We are very grateful to Drs Frank Schmitz (Homburg, Saar, Germany) and Wiebke Möbius (Göttingen, Germany) for generous help with electron microscopy. Expert technical assistance was provided by Markus Jahn, Elke Redecker, and Michael Pilot. The work on synaptic vesicle endocytosis including electron microscopy was designed, performed, and analyzed by the group of JK, and supported by grants from the Deutsche Forschungsgemeinschaft (SFB 523) and the HFSP to JK. The group of JW is supported by the Deutsche Forschungsgemeinschaft through SFB 549 and FOR 521.

References

Benesch S, Polo S, Lai FP, Anderson KI, Stradal TE, Wehland J, Rottner K (2005) N-WASP deficiency impairs EGF internalization and actin assembly at clathrin-coated pits. *J Cell Sci* **118:** 3103–3115

Betz WJ, Bewick GS (1992) Optical analysis of synaptic vesicle recycling at the frog neuromuscular junction. *Science* **255:** 200–203

Danino D, Hinshaw JE (2001) Dynamin family of mechanoenzymes. *Curr Opin Cell Biol* **13:** 454–460

Di Paolo G, Sankaranarayanan S, Wenk MR, Daniell L, Perucco E, Caldarone BJ, Flavell R, Picciotto MR, Ryan TA, Cremona O, De Camilli P (2002) Decreased synaptic vesicle recycling efficiency and cognitive deficits in amphiphysin 1 knockout mice. *Neuron* **33:** 789–804

Ensenat D, Yao Z, Wang XS, Kori R, Zhou G, Lee SC, Tan TH (1999) A novel Src homology 3 domain-containing adaptor protein, HIP-55, that interacts with hematopoietic progenitor kinase 1. *J Biol Chem* **274:** 33945–33950

Fenster SD, Kessels MM, Qualmann B, Chung WJ, Nash J, Gundelfinger ED, Garner CC (2003) Interactions between piccolo and the actin/dynamin-binding protein Abp1 link vesicle endocytosis to presynaptic active zones. *J Biol Chem* **278:** 20268–20277

Giovedi S, Vaccaro P, Valtorta F, Darchen F, Greengard P, Cesareni G, Benfenati F (2004) Synapsin is a novel Rab3 effector protein on small synaptic vesicles. I. Identification and characterization of the synapsin I–Rab3 interactions *in vitro* and in intact nerve terminals. *J Biol Chem* **279:** 43760–43768

Han J, Kori R, Shui JW, Chen YR, Yao Z, Tan TH (2003) The SH3 domain-containing adaptor HIP-55 mediates c-Jun N-terminal kinase activation in T cell receptor signaling. *J Biol Chem* **278:** 52195–52202

Han J, Shui JW, Zhang X, Zheng B, Han S, Tan TH (2005) HIP-55 is important for T-cell proliferation, cytokine production, and immune responses. *Mol Cell Biol* **25:** 6869–6878

Heuser JE, Reese TS (1973) Evidence for recycling of synaptic vesicle membrane during transmitter release at the frog neuromuscular junction. *J Cell Biol* **57:** 315–344

Hilfiker-Kleiner D, Hilfiker A, Fuchs M, Kaminski K, Schaefer A, Schieffer B, Hillmer A, Schmiedl A, Ding Z, Podewski E, Podewski E, Poli V, Schneider MD, Schulz R, Park JK, Wollert KC, Drexler H (2004) Signal transducer and activator of transcription 3 is required for myocardial capillary growth, control of interstitial matrix deposition, and heart protection from ischemic injury. *Circ Res* **95:** 187–195

Hirst J, Robinson MS (1998) Clathrin and adapters. *Biochim Biophys Acta* **1404:** 173–193

Holtzman D, Yang S, Drubin D (1993) Synthetic-lethal interactions identify two novel genes, SLA1 and SLA2, that control membrane cytoskeleton assembly in *Saccharomyces cerevisiae*. *J Cell Biol* **122:** 635–644

Hyun TS, Li L, Oravecz-Wilson KI, Bradley SV, Provot MM, Munaco AJ, Mizukami IF, Sun H, Ross TS (2004) Hip1-related mutant mice grow and develop normally but have accelerated spinal abnormalities and dwarfism in the absence of HIP1. *Mol Cell Biol* **24:** 4329–4340

Kessels MM, Engqvist-Goldstein AEY, Drubin DG (2000) Association of mouse actin-binding protein 1 (mAbp1/SH3P7), an Src kinase target, with dynamic regions of the cortical actin cytoskeleton in response to Rac1 activation. *Mol Biol Cell* **11:** 393–412

Kessels MM, Engqvist-Goldstein AEY, Drubin DG, Qualmann B (2001) Mammalian Abp1, a signal-responsive F-actin-binding protein, links the actin cytoskeleton to endocytosis via the GTPase dynamin. *J Cell Biol* **153:** 351–366

Kim WT, Chang S, Daniell L, Cremona O, Di Paolo G, De Camilli P (2002) Delayed reentry of recycling vesicles into the fusion-competent synaptic vesicle pool in synaptojanin 1 knockout mice. *Proc Natl Acad Sci USA* **99:** 17143–17148

Kirchhausen T (1999) Adaptors for clathrin-mediated traffic. *Annu Rev Cell Dev Biol* **15:** 705–732

Klingauf J, Kavalali ET, Tsien RW (1998) Kinetics and regulation of fast endocytosis at hippocampal synapses. *Nature* **394:** 581–585

Lappalainen P, Kessels MM, Cope M, Drubin DG (1998) The ADF homology (ADF-H) domain: a highly exploited actin-binding module. *Mol Biol Cell* **9:** 1951–1959

Larbolette O, Wollscheid B, Schweikert J, Nielsen PJ, Wienands J (1999) SH3P7 is a cytoskeleton adapter protein and is coupled to signal transduction from lymphocyte antigen receptors. *Mol Cell Biol* **19:** 1539–1546

Le Bras S, Foucault I, Foussat A, Brignone C, Acuto O, Deckert M (2004) Recruitment of the actin-binding protein HIP-55 to the immunological synapse regulates T cell receptor signaling and endocytosis. *J Biol Chem* **279:** 15550–15560

Lila T, Drubin DG (1997) Evidence for physical and functional interactions among two *Saccharomyces cerevisiae* SH3 domain proteins, an adenylyl cyclase-associated protein and the actin cytoskeleton. *Mol Biol Cell* **8:** 367–385

Lock P, Abram CL, Gibson T, Courtneidge SA (1998) A new method for isolating tyrosine kinase substrates used to identify Fish, an SH3 and PX domain-containing protein, and Src substrate. *EMBO J* **17:** 4346–4357

Marsh M, McMahon HT (1999) Cell biology—the structural era of endocytosis. *Science* **285:** 215–220

Merrifield CJ, Perrais D, Zenisek D (2005) Coupling between clathrin-coated-pit invagination, cortactin recruitment, and membrane scission observed in live cells. *Cell* **121:** 593–606

Mise-Omata S, Montagne B, Deckert M, Wienands J, Acuto O (2003) Mammalian actin binding protein 1 is essential for endocytosis but not lamellipodia formation: functional analysis by RNA interference. *Biochem Biophys Res Commun* **301:** 704–710

Morris RG (1989) Synaptic plasticity and learning: selective impairment of learning rats and blockade of long-term potentiation *in vivo* by the *N*-methyl-D-aspartate receptor antagonist AP5. *J Neurosci* **9:** 3040–3057

Newpher TM, Smith RP, Lemmon V, Lemmon SK (2005) *In vivo* dynamics of clathrin and its adaptor-dependent recruitment to the actin-based endocytic machinery in yeast. *Dev Cell* **9:** 87–98

Olivo-Marin JC (2002) Extraction of spots in biological images using multiscale products. *Pattern Recogn* **35:** 1989–1996

©2006 European Molecular Biology Organization

Peter BJ, Kent HM, Mills IG, Vallis Y, Butler PJ, Evans PR, McMahon HT (2004) BAR domains as sensors of membrane curvature: the amphiphysin BAR structure. *Science* **303:** 495–499

Qualmann B, Boeckers TM, Jeromin M, Gundelfinger ED, Kessels MM (2004) Linkage of the actin cytoskeleton to the postsynaptic density via direct interactions of Abp1 with the ProSAP/Shank family. *J Neurosci* **24:** 2481–2495

Richards DA, Guatimosim C, Betz WJ (2000) Two endocytic recycling routes selectively fill two vesicle pools in frog motor nerve terminals. *Neuron* **27:** 551–559

Ryan TA, Li L, Chin LS, Greengard P, Smith SJ (1996) Synaptic vesicle recycling in synapsin I knock-out mice. *J Cell Biol* **134:** 1219–1227

Ryan TA, Smith SJ (1995) Vesicle pool mobilization during action potential firing at hippocampal synapses. *Neuron* **14:** 983–989

Seidman JG, Seidman C (2001) The genetic basis for cardiomyopathy: from mutation identification to mechanistic paradigms. *Cell* **104:** 557–567

Seki N, Muramatsu M, Sugano S, Suzuki Y, Nakagawara A, Ohhira M, Hayashi A, Hori T, Saito T (1998) Cloning, expression analysis, and chromosomal localization of HIP1R, an isolog of huntingtin interacting protein (HIP1). *J Hum Genet* **43:** 268–271

Slepnev VI, De Camilli P (2000) Accessory factors in clathrin-dependent synaptic vesicle endocytosis. *Nat Rev Neurosci* **1:** 161–172

Sparks AB, Hoffman NG, McConnell SJ, Fowlkes DM, Kay BK (1996) Cloning of ligand targets: systematic isolation of SH3 domain-containing proteins. *Nat Biotechnol* **14:** 741–744

Stevens CF, Williams JH (2000) 'Kiss and run' exocytosis at hippocampal synapses. *Proc Natl Acad Sci USA* **97:** 12828–12833

Takei K, Mundigl O, Daniell L, De Camilli P (1996) The synaptic vesicle cycle: a single vesicle budding step involving clathrin and dynamin. *J Cell Biol* **133:** 1237–1250

Takei K, Slepnev VI, Haucke V, De Camilli P (1999) Functional partnership between amphiphysin and dynamin in clathrin-mediated endocytosis. *Nat Cell Biol* **1:** 33–39

Wesp A, Hicke L, Palecek J, Lombardi R, Aust T, Munn AL, Riezman H (1997) End4p/Sla2p interacts with actin-associated proteins for endocytosis in *Saccharomyces cerevisiae*. *Mol Biol Cell* **8:** 2291–2306

Yang S, Cope MJ, Drubin DG (1999) Sla2p is associated with the yeast cortical actin cytoskeleton via redundant localization signals. *Mol Biol Cell* **10:** 2265–2283

Yarar D, Waterman-Storer CM, Schmid SL (2005) A dynamic actin cytoskeleton functions at multiple stages of clathrin-mediated endocytosis. *Mol Biol Cell* **16:** 964–975

 ©2006 European Molecular Biology Organization